Stress Evolution and Creep Deformation in Solid-Oxide Electrolysis Cell Systems – Dynamic Modeling and Multi-Objective Optimization to Maximize Stack Life and Efficiency

Nishant V. Giridhar[1a], Quang Minh Le[1a], Debangsu Bhattacharyya[1*]

Doug A. Allan[2,3], Eric Liese[4], Stephen E. Zitney[1,4]

[1] Department of Chemical and Biomedical Engineering, West Virginia University, Morgantown, WV 26506, USA

[2] NETL, Pittsburgh, PA 15236, USA

[3] NETL Site Support Contractor, Pittsburgh, PA 15236, USA

[4] National Energy Technology Laboratory (NETL), Morgantown, WV 26507, USA

[a] These authors contributed equally to this paper.

Abstract

This study develops a thermal stress model of solid-oxide electrolysis cells (SOECs) including a model for creep strain and failure probability and integrates that with a dynamic plant-wide model of a hydrogen production process. Uncertainties in key material properties of the cell are quantified to assess their impact on stress profile variability. The oxygen electrode is found to have about 10 times higher failure probability compared to the fuel electrode. The study shows that if the stack operation is not optimized, cycling operation would lead to stress build-up eventually leading to catastrophic failure. A dynamic optimization problem is set up for obtaining the optimal operational profile considering variable hydrogen production rate. Due to the tradeoff between the efficiency and stress build-up, the dynamic optimization problem is multi-objective. It is observed that the optimizer can considerably reduce the stress build-up (i.e., can increase the stack life) albeit at the cost of a lower efficiency thus exhibiting strong tradeoffs between capital and operating costs. For example, if the stack would be replaced in 0.5 yr, specific energy requirement would be 48.5 kWh/kg H_2 while for a stack replacement time of about 6 yr, the specific energy requirement rises by about 4.2%.

Keywords: SOEC, thermal stress, uncertainty quantification, dynamic optimization

1. Introduction

Hydrogen is a carbon-free energy carrier with extensive current and potential uses in the power and chemical industries. Hydrogen can be produced by using electrolysis using renewably sourced power thus also helping higher penetration of renewables into the electric grid without adversely affecting the grid reliability and affecting dynamics of non-renewable energy sources. One potential technology to producing hydrogen is by using solid-oxide electrolysis cells (SOECs) that offer high efficiency [1]. However, their high-temperature operation, necessary for realizing the high efficiency, can degrade cell components, causing irreversible structural damage and performance loss. There are four main types of thermo-mechanical degradation in SOECs [2]: residual stress or strain from manufacturing, thermal stress or strain, creep strain from prolonged high-temperature operation, and chemical expansion effects coupled with electrochemical-mechanical interactions.

Recent solid-oxide cell (SOC) research has focused extensively on the challenges posed by thermal stress due to high operating temperatures and thermal gradients. Much of the work in this area has focused on solid-oxide fuel cells (SOFCs) rather than SOECs. Chiang *et al.* [3] focused on thermal stresses in an anode-supported SOFC under various operating conditions. Their results showed that principal stresses increase when temperature gradients increase. The study also showed that preheating of the inlet gas reduces temperature gradients and consequently thermal stress. Peng *et al.* [4] have noted that thermal stresses can cause severe performance degradation and eventual rupture of critical cell components. To address this issue, the impact of design geometries for planar SOFCs has been extensively evaluated particularly focusing on the thickness of the electrode layer and the design of gas flow channels. Liu *et al.* [5] developed a mathematical model to estimate thermal stresses in planar SOFCs, particularly under thermal cycling conditions. Their findings indicate that increasing electrolyte thickness leads to a reduction in the number of cycles before failure. The work of Colombo *et al.* [6] showed that the aging process is highly impacted by the operational history, including the number of duty cycles, frequency, and the severity of thermal cycling. Xu *et al.* [7] explored the possibility of controlling temperature gradients through operational adjustments. There are several other notable works in this area, again all focusing on SOFCs (Wang *et al.*, 2018; [8].

Creep deformation during long-term operation can be a significant factor leading to both electrochemical performance degradation and mechanical failure of SOFCs. Greco *et al.* [9] studied the impact of anode and sealant creep over 10,000 hours, particularly focusing on stress redistribution and its implications for the mechanical survival of the repeating unit under lower current densities. They also studied the thermo-mechanical reliability of SOFC stacks during extended operation, and found that there is a substantial decrease in contact pressure due to creep deformation [10]. Peksen [11] reported how creep strain over prolonged periods can cause high deformation in metal components. Wang *et al.* [12] studied the effect of frame creep parameters on the long-term mechanical performance of SOFCs under isothermal conditions. Guo and Lin [13] performed a comprehensive thermo-mechanical analysis using a multiphysics model to assess the impact of creep on the mechanical degradation of all SOFC components over 10,000 hours. Luo *et al.* [14] focused on a creep analysis of tubular SOFCs, studying the effect of tube radius on stress distribution. Their results showed that the hoop stress of the electrolyte increases with the increase in the radius of the tube for tubular SOFCs. Zhang *et al.* [15] used a probabilistic model for creep damage to evaluate the evolution of failure probability in SOFCs with varying geometric dimensions during the creep process. They found that increasing the thickness or width of the sealant and decreasing the thickness of the anode

and frame can reduce the failure probability of the glass-ceramic sealant. Despite the growing number of studies on the long-term mechanical failure of SOFCs, a common limitation in these studies is the assumption of isothermal conditions. This simplification often leads to the consideration of the creep effect of only one or a few materials/components in the SOFC, rather than a comprehensive assessment of the entire cell under realistic operating conditions. Furthermore, most studies have focused on thermal stress analysis of SOECs. Recently, Sun *et al.* [16] performed a study on thermal stress evolution in SOECs. There is scarcity of studies in the open literature on thermal stress analysis of SOECs, especially under non-isothermal operation. It should be noted that a model for the thermal stress evolution considering creep strain has been developed by Zhao *et al.* [17]. However, their model is applicable for systems when temperature change with time is negligible. However, as H2 production rate varies with time and cell transitions from the endothermic mode to the exothermic mode and vice versa, spatio-temporal change in cell/stack temperature is practically unavoidable. The model developed in this work takes into account the impact of spatio-temporal change in cell/stack temperature on the evolution of thermal stress and creep strain. Understanding the impact of non-isothermal operation of SOECs under varying load conditions on stress evolution is important to prolong the cell life, which would not only reduce the capital expenses but would also improve the reliability. .

Recent studies have highlighted the significant impact of balance of plant (BOP) operation on the performance and physical integrity of SOCs. Notably, the thermal dynamics within SOECs are influenced not only by energy generation (such as Ohmic losses) and consumption (from endothermic reactions) within the cells but also by thermal transients in the BOP, which impact the dynamics of cell inlet temperatures. Only a few studies in the open literature have investigated the impact of BOP on thermal stress evolution in SOEC or SOFC systems. Colombo *et al.* [18] used a multiphysics modeling approach to evaluate the performance and thermal stresses in SOFCs under steady-state and transient conditions. The same authors [19] also investigated the dynamics of air/fuel ratio, fuel channel pressure, and mean solid temperature on the failure probability. In addition, Colombo and Kharton [20] investigated the start-up of SOFCs at both component and system levels, concluding that the electrolyte experiences the highest stress due to its higher Young's modulus compared to that of the electrodes. The same authors[6] proposed a set of design and operational guidelines for addressing failure and degradation risks of SOFCs in micro-grid applications. Liu *et al.* (Liu *et al.*, 2022) developed a dynamic model for a reversible solid-oxide cell (rSOC) and the BOP to explore the effects of various operating conditions on the maximum positive-electrolyte-negative temperature and maximum temperature gradient. However, evolution of thermal stress in various SOEC components and failure analysis were not studied. Overall, there is a significant gap in the research literature regarding stress and failure probability analysis of SOECs considering non-isothermal models and BOP dynamics. It is important to note that thermal dynamics within SOECs differ significantly from those in SOFCs. SOFCs consistently operate under exothermic conditions, regardless of operating parameters, as both Ohmic losses and reactions are exothermic. In contrast, SOECs can operate under either endothermic or exothermic conditions depending on the operating voltage. When operating below the thermo-neutral voltage (i.e., lower hydrogen production rates), the process is endothermic, whereas above the thermo-neutral voltage, it becomes exothermic. These variations significantly affect temperatures and stress dynamics as the load changes. This is further influenced by the dynamics of BOP equipment items [21].

Many authors have focused on steady-state optimization of SOFCs to enhance their performance, efficiency, and economic feasibility [22]. These studies span from optimizing physical dimensions and

operating conditions to minimizing lifecycle costs and improving overall system robustness under uncertainties. For example, Feng *et al.* [23] maximized the power output of a single tubular SOFC by considering the optimal thickness of the cathode and the length of the fuel cell for a given inner radius as the decision variables. Bhattacharyya *et al.* [24] utilized a multi-objective optimization method to maximize both gravimetric and volumetric power densities of a tubular SOFC. Cheddie [25] minimized the lifecycle specific energy cost of an SOFC power plant. This was achieved by optimizing the SOFC size and the operating conditions such as the molar flow rates of methane and oxygen, as well as the recycling fraction of the SOFC anode outlet. Spivey *et al.* [26] minimized the total annual operating cost of an SOFC while ensuring compliance with cell lifetime constraints. Gholaminezhad *et al.* [27] conducted multi-objective optimization for methane-fueled SOFCs, considering both microstructural and operational factors to maximize system efficiency and power density. Ferreira *et al.* [28] and Rauh [29] investigated the real-time optimization of an SOFC system.

Compared to the extensive literature on the optimization of SOFC systems, literature focusing on the optimization of SOEC systems remains scarce. Yin *et al.* [30] investigated the importance of temperature management in SOEC systems, particularly during the transition between thermoneutral and exothermic modes in response to external and internal changes. Their work emphasized the need for developing strategies to maintain optimal performance. Cai *et al.* [31] developed optimal control of SOECs.

Although operational optimization has been widely used to address the mitigation of chemical and performance degradation [1,32–34], studies on physical degradation has mainly considered improvements in design and manufacturing. Studies such as Wang *et al.* [35] have combined the finite element method with the response surface method for optimizing dimensions of SOFCs for minimizing sealant failure probability. From an operational optimization perspective, Cheng *et al.* [36] focused on maximizing efficiency under a temperature constraint. Li *et al.* [37] incorporated mixed partial temperature gradients as a surrogate for thermal-stress in a control study focused on mode-switching dynamic operation. To the best of our knowledge, there is currently no work in the open literature on dynamic optimization of hydrogen production systems using non-isothermal SOEC stacks with explicit consideration of spatio-temporal evolution of stress as hydrogen production rates vary. This paper seeks to fill in these gaps. We make the following contributions:

- A thermal stress model is developed for an SOC and validated with literature data. This stress model is then included in a plant-wide dynamic model of a hydrogen generation process that considers non-isothermal operation of the SOEC stack along with the BOP.
- Uncertainties in spatio-temporal evolution of stress due to uncertainties in thermo-mechanical properties of cell component materials are analyzed.
- The integrated modeling framework is used for equation-oriented dynamic optimization of SOEC systems under flexible operation by taking into account the tradeoffs between efficiency and structural reliability of the SOEC.

This study offers a first step towards computational framework that integrates thermal stress and creep deformation modeling with a system level plantwide model. Given a sufficiently characterized cell design with well-defined material properties and a standard planar structure, the stress modeling and optimization-based decision-making framework developed in this work can be adapted to different cell constructions that are known to have significant variations from manufacturer to manufacturer. While this work quantifies the uncertainty in the material properties available in the literature, we emphasize that

online application of this framework requires the adaptation of the model parameters to the specific materials used in the actual cells. Another key assumption that we make is that each layer of the multi-layered PEN structure is uniform. Experimental characterization studies on the creep deformation of construction materials have shown that creep rates are negatively correlated with the coefficient of uniformity in the material[38]. However, similar studies for SOC electrode and electrolyte materials are not available. The SOC model used in this work can be expanded to provide more spatial resolution, but the computational tractability of the multi-objective dynamic optimization problem should be investigated.

This work ignores detailed stack-level interactions, rather approximates it by modeling a central cell with boundary conditions for heat loss, providing a tractable representation for dynamic optimization. While more detailed stack models, including inter-cell coupling and statistical approaches such as the Fokker-Planck equation, offer valuable insights, such granular representation can lead to intractability of the underlying dynamic optimization problem undertaken in this work, that focuses on system-level optimization.

It should also be noted that operational optimization is only one method of increasing the usable life of an SOC stack. The thermal performance of SOC structure can significantly be improved by advances in manufacturing techniques and selection of electrode materials and morphology. Recent theoretical and experimental studies have found that incorporating LSCO nanoparticles into similar composite materials results in an improved strength of the microstructure[39]. However, further studies are necessary for compatibility and technical/economic viability of these materials for SOC stacks. Finally, many studies have addressed the practice of breaking in or condition electrochemical cells before they are deployed. A recent review by Moghaddam *et al.*[40] details various conditioning practices employed for PEMFC stacks particularly for automotive applications that typically involve load cycling. Similar approaches can be investigated for the high temperature operation of SOECs in addition to the operational strategies investigated in this system-level optimization study.

2. Methodology

2.1 Solid-oxide electrolysis cell

Figure 1(a) shows a planar solid-oxide cell that consists of two electrodes separated by a thin electrolyte. In the context of this work, we adopt the terms fuel electrode and oxygen (O_2) electrode instead of anode and cathode as these terms are ambiguous when dealing with reversible solid-oxide cells. In this study, the fuel electrode is composed of a Ni-YSZ cermet material while the oxygen electrode is composed of LSM-YSZ composite. The two electrodes are separated by a YSZ oxygen ion conducting electrolyte. While Figure 1 shows two electrodes of equal thickness, in practice the fuel electrode is significantly thicker and acts as the support. The thickness and materials of construction of each of the three layers plays a significant role in determining the distribution of thermal stresses in the cell.

A 2-D non-isothermal dynamic SOC model was developed in previous studies (Bhattacharyya *et al.*, 2009) and recently expanded by some of the authors of this paper in a recent publication [37]. The model includes spatially distributed mass and energy balances in addition to a detailed electrochemical model. The current version of the model that is used in this work has been developed in the open-source equation-oriented IDAES (Institute for the Design of Advanced Energy Systems) modeling and optimization platform [41]. Each cell in the stack is a planar fuel electrode supporting cell with a length of 23.5 cm in the *z*-direction and assumes countercurrent fuel and oxidant channel flow. The cell operates counter currently, with periodic boundary conditions representing interconnects connecting the top of the fuel channel to the

bottom of the oxygen channel, simulating a central cell in a large stack. Environmental losses are neglected due to their minimal impact. The model is 1-D for the channels, electrodes, and the electrolyte while the fuel electrode is modeled by one finite element in the *x*-direction. The fuel electrode has a thickness of 0.1 cm while the oxygen electrode and the electrolyte are assumed to be thin layers.

2.2 SOEC Flowsheet

The SOEC described above is integrated into a dynamic hydrogen (H_2) production flowsheet, as shown in Figure 1(b), that consists of recuperative heat exchangers, feed and sweep trim heaters, in addition to other equipment items such as a blower for the air stream. The oxygen exhaust is vented while the fuel exhaust passes through a condenser and flash vessel to separate water before being removed as the product. In addition to the BOP equipment, the dynamic flowsheet also consists of a traditional control system that has been developed and tuned for setpoint transitions. Further details about the flowsheet and the control system can be found in a previous work [37].

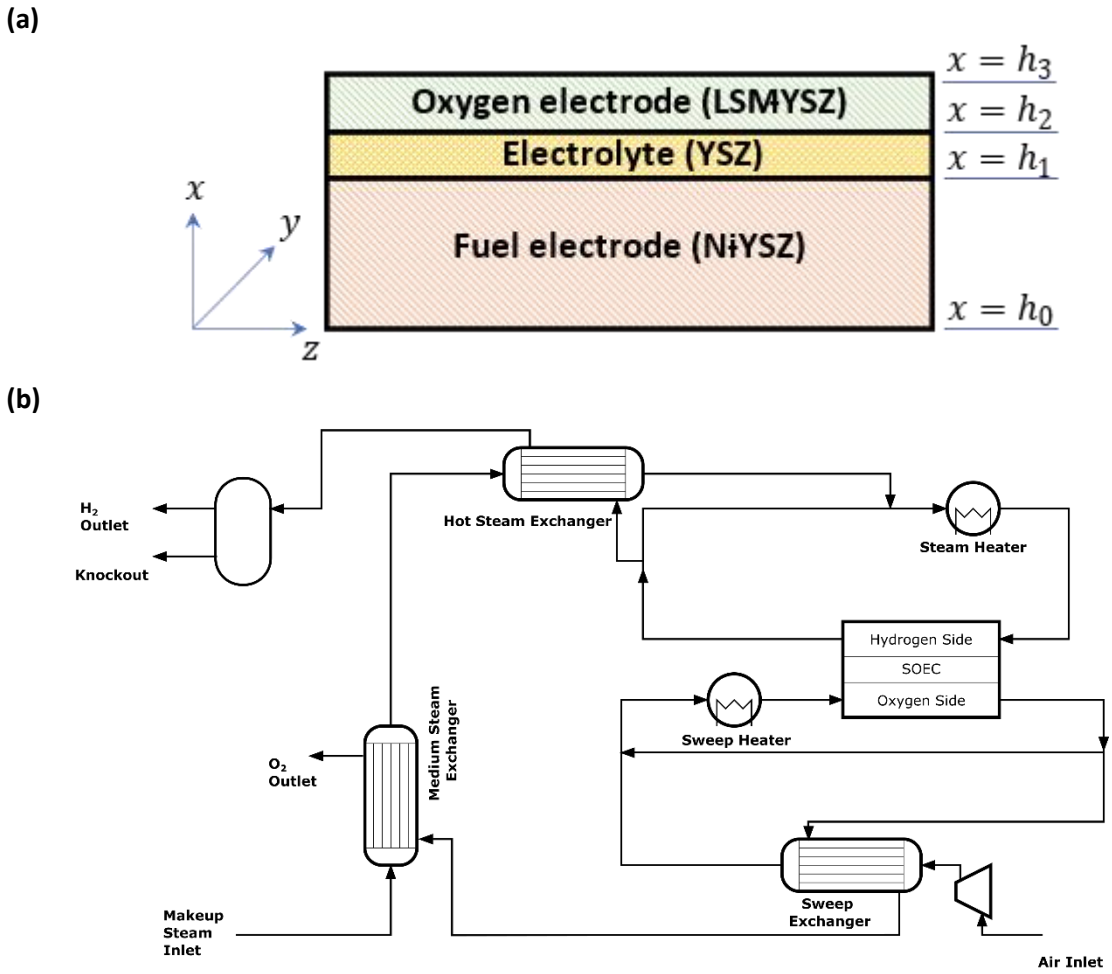

Figure 1. (a) Multi-layered structure of Fuel Electrode supported Planar SOEC and (b) general schematic diagram of the SOEC-based H_2 production plant consisting of the SOEC stack and Balance-of-plant.

2.3 Thermal stress model

In this model, the SOEC is considered to bend freely [42]. Thermal stresses are calculated for an elastic multilayered system, as detailed in Figure 1(a) This study assumes:

- The Euler-Bernoulli assumption[43] (i.e., that the plane section remains plane under lateral deformation) holds and thus the transverse shear stress is not accounted for.
- All layers are assumed to be elastic and isotropic and have a uniform morphology.
- Furthermore, the most common type of SOECs is the fuel electrode supported (Ni-YSZ) and so the thickness of that electrode is much higher than the electrolyte and oxygen electrode. Therefore, the fuel electrode is considered to be the substrate while other layers are considered to be films.
- There is no external load.
- Due to typical cell enclosure/construction, displacement in the width direction is ignored.

Under the assumptions stated above, the axial force equilibrium for the *n*-layer system can be written as[17,43]:

$$\sum_{i=1}^{n} \int_{A} \sigma_{i,xx} dA = 0 \tag{1}$$

,where σ_i denotes the stress in the *i*th layer and $dA = dx\, dy$

By using the generalized Hooke's law, considering time-dependent deformation due to creep strain, under assumption that the axial displacement is a linear function of only the coordinate x in the plane of the cross-section of the multi-layered system (see the last assumption listed above), and applying the theory of linear thermo-elasticity, we get:

$$\varepsilon(x,t) = \varepsilon_0(t) + k(t)x \tag{2}$$

$$\sigma_i(x,t) = M_i[\varepsilon_0(t) + k(t)x - \alpha_i \nabla T_i(x,t) - \varepsilon_i^{cr}(x,t)] \tag{3}$$

, where $M_i = \frac{E_i}{(1-\vartheta_i)}$

In Eqs. (2) and (3), t denotes time, E_i , ϑ_i , and α_i are the Young's modulus, Poisson's ratio, and coefficient of thermal expansion for the material in the *i*th layer, respectively, k denotes the curvature of the neutral axis, $\varepsilon_0(t)$ denotes the reference strain at the bottom surface of the substrate, ε_i^{cr} and ∇T_i denote the creep strain and temperature difference of the *i*th layer, respectively.

Given the assumptions noted before and under Euler-Bernoulli assumption[43], Eq. (1) yields:

$$\sum_{i=1}^{n} \int_{h_{i-1}}^{h_i} \sigma_i(x,t) dx = 0 \tag{4}$$

Substituting Eqs. (2) and (3) in Eq. (4), and taking partial integration, it yields:

$$C_1\varepsilon_0(t) + C_2k(t) - \sum_{i=1}^{n}\int_{h_{i-1}}^{h_i} M_i\,\alpha_i\nabla T_i(x,t)dx - \sum_{i=1}^{n}\int_{h_{i-1}}^{h_i} M_i\,\varepsilon_i^{cr}(x,t)dx = 0 \tag{5}$$

where:

$$C_1 = \sum_{i=1}^{n} M_i t_i \tag{6}$$

, with $t_i = h_i - h_{i-1}$, denotes the thickness of the i^{th} layer.

$$C_2 = \frac{1}{2}\sum_{i=1}^{n} M_i\left(h_i^2 - h_{i-1}^2\right) \tag{7}$$

Taking the derivative of Eq. (5) with respect to time and defining variables *R* and *P* as:

$$R = \sum_{i=1}^{n}\int_{h_{i-1}}^{h_i} M_i\,\alpha_i\dot{\nabla}T_i(x,t)dx \tag{8}$$

$$P = \sum_{i=1}^{n}\int_{h_{i-1}}^{h_i} M_i\dot{\epsilon}_i^{cr}(x,t)dx \tag{9}$$

,we obtain:

$$\dot{\varepsilon_0}(t) + \frac{C_2}{C_1}\dot{k}(t) - \frac{R}{C_1} - \frac{P}{C_1} = 0 \tag{10}$$

$$\frac{C_1}{C_2}\dot{\varepsilon_0}(t) + \dot{k}(t) - \frac{R}{C_2} - \frac{P}{C_2} = 0 \tag{4}$$

Given the assumptions stated before, bending moment equilibrium of the SOC cell can be written as [17,43]:

$$\sum_{i=1}^{n}\int_{h_{i-1}}^{h_i}\sigma_i(x,t)xdx = 0 \tag{5}$$

Substituting Eqs. (2) and (3) in Eq. (12), and taking partial integration, it yields:

.

$$C_2\varepsilon_0(t) + C_3k(t) - \sum_{i=1}^{n}\int_{h_{i-1}}^{h_i} M_i\,\alpha_i\nabla T_i(x,t)xdx - \sum_{i=1}^{n}\int_{h_{i-1}}^{h_i} M_i\,\varepsilon_i^{cr}(x,t)xdx = 0 \tag{13}$$

where:

$$C_3 = \frac{1}{3}\sum_{i=1}^{n} M_i\left(h_i^3 - h_{i-1}^3\right) \tag{6}$$

Taking the derivative of Eq. (13) with respect to time and defining variables *S* and *Q* as:

$$S = \sum_{i=1}^{n}\int_{h_{i-1}}^{h_i} M_i\,\alpha_i\dot{\nabla} T_i(x,t)xdx \tag{7}$$

$$Q = \sum_{i=1}^{n}\int_{h_{i-1}}^{h_i} M_i\,\dot{\varepsilon}_i^{cr}(x,t)xdx \tag{8}$$

, we obtain:

$$\dot{\varepsilon_0}(t) + \frac{C_3}{C_2}\dot{k}(t) - \frac{S}{C_2} - \frac{Q}{C_2} = 0 \tag{9}$$

$$\frac{C_2}{C_3}\dot{\varepsilon_0}(t) + \dot{k}(t) - \frac{S}{C_3} - \frac{Q}{C_3} = 0 \tag{10}$$

Subtracting Eq. (17) from Eq. (10) and after some algebraic manipulation, we obtain :

$$\dot{k}(t) = \frac{RC_2 - SC_1 + PC_2 - QC_1}{C_2^2 - C_1C_3} \tag{11}$$

Subtracting Eq. (18) from Eq. (11) and after some algebraic manipulation, we obtain:

$$\dot{\varepsilon_0}(t) = \frac{RC_3 - SC_2 + PC_3 - QC_2}{C_1C_3 - C_2^2} \tag{20}$$

Under constant stress and temperature, many materials have been observed to undergo three stages- primary, secondary and tertiary. If the state of stress becomes invariant with time, then the material reaches stationary regime where the components experience creep in a stationary state. Both primary and stationary creeps are generally given by the power law [43]:

$$\dot{\varepsilon_i^{cr}}(x,t) = A_i\sigma_i^{n_i}(x,t) \tag{12}$$

, where A_i and n_i denote the creep constant and exponent, respectively for the i[th] layer.

Taking derivative of Eqs. (2) and (3), we obtain:

$$\dot{\varepsilon}(x,t) = \dot{\varepsilon_0}(t) + \dot{k}(t)x \tag{13}$$

$$\dot{\sigma_i}(x,t) = E_i^*\left[\dot{\varepsilon_0}(t) + \dot{k}(t)x - \alpha_i\dot{\nabla}T_i(x,t) - \dot{\varepsilon_i^{cr}}(x,t)\right] \tag{14}$$

Eqs. (19), (20), (21), (22), and (23) are solved along with the SOC-based plant model equations to obtain stress and strain profiles with time. To solve these differential equations, consistent initial conditions are required. It is assumed that the sintering temperature during manufacturing of the cell is the reference temperature, i.e., the cell is stress-free and strain-free, but as it is brought to the operating temperature that is lower than the sintering temperature, it would develop stress, but with sufficient time, denoted by t_{suf} the stress would relax. Thus, the initial condition of the cells for this work is considered to be stress free, but with non-zero strain. Therefore, the following set of equations are solved to obtain the consistent initial conditions:

$$\varepsilon_0(t=0) = \varepsilon_0\left(t_{suf}\right) \tag{15}$$

$$k(0) = k\left(t_{suf}\right) \tag{16}$$

$$\varepsilon_i^{cr}(0,x) = \varepsilon_i^{cr}\left(t_{suf},x\right) \tag{17}$$

$$\dot{\varepsilon}\left(x,t_{suf}\right) = \dot{\varepsilon_0}\left(t_{suf}\right) + \dot{k}\left(t_{suf}\right)x = 0 \tag{18}$$

$$\sigma_i\left(x,t_{suf}\right) = 0 \tag{19}$$

$$\varepsilon_i(x, t_{suf}) - \alpha_i \nabla T(x, t_{suf}) - \varepsilon_i^{cr}(x, t_{suf}) = 0 \quad (20)$$

$$\varepsilon_0(t_{suf}) + k(t_{suf})x - \alpha_i \nabla T(x, t_{suf}) - \varepsilon_i^{cr}(x, t_{suf}) = 0 \quad (30)$$

, where ∇T denotes the difference between initial operating temperature and the sintering temperature for generating these initial conditions.

2.4 Failure probability analysis

In SOCs, electrolyte, anode, and cathode, are ceramic materials. Ceramics are more susceptible to failure due to tensile stress rather than compressive stress. However, given the multi-layered structure of SOCs and the high operating temperature and expected high spatio-temporal temperature gradient, it is important to ensure that the compressive stress remains below the acceptable level [44].

Failures of ceramics are uncertain. Failure probabilities for ceramic materials can be assumed to be independent of time for simplicity, but this requires ignoring time-varying crack growth probability. In this work failure probability is considered to be time-dependent to account for long-term, high-temperature SOC operations that leads to creep deformation, a key failure mechanism in these conditions, causing new cracks or exacerbating existing defects.

The Weibull distribution given by Eq. (31) is often used for estimating materials failure probability [45,46]:

$$F(t) = 1 - exp\left[-\left(\frac{\sigma(t)}{\sigma_0}\right)^m \frac{V(t)}{V_0}\right] \quad (21)$$

where F is the failure probability, , σ_0 IS the characteristic strength, m is the Weibull modulus, V_j is the volume of the material, and V_0 is the reference volume associated with the characteristic strength. The Weibull distribution has been widely applied to metals. Unlike metals, ceramics do not have a constant creep failure strain, due to the uncertainty in flaw size, structure, and stress distribution[15]. Instead of Equation (31), a modified form of the Weibull distribution[15] given by Eq. (32) is used. This modified form is given in terms of strain ε and characteristic strain ε_0. The characteristic Weibull distribution parameters m, ε_0, and V_0 depends on the materials of construction of a layer:

$$F(t) = 1 - exp\left[-\left(\frac{\varepsilon(t)}{\varepsilon_0}\right)^m \frac{V(t)}{V_0}\right] \quad (22)$$

The change in the characteristic volume $V(t)$ for any finite element can be related to the strain $\varepsilon(t)$ by considering any change in volume to be additive as per:

$$V(t) = V_0 + \Delta V(t) \quad (23)$$

The strain is typically defined as shown in Eq. (34).

$$\varepsilon(t) = \frac{\Delta L(t)}{L_0} \tag{24}$$

Considering a regular cube, $V \propto L^3$, we obtain:

$$\frac{V(t)}{V_0} = 1 + \varepsilon^3 \tag{25}$$

2.5 Dynamic optimization

During transient operation of the SOEC, temperature fluctuations and high-temperature operation can be unavoidable. Consequently, over the span of long-term operation, creep deformation is inevitable and will lead to eventual failure. For the reliability of a H_2-production system, the stack should be replaced before a certain failure probability is reached. In this study, the replacement time for the stack is considered to be the time when the failure probability reaches 60%. To evaluate long term evaluation of stress, strain and failure probability, we use the following approach to keep the computational cost tractable:

1) Dynamic optimization is performed over a single 8-hour cycle and then the cycle is assumed to be repeated over the plant lifetime. Obviously, cycles of longer duration and with varying operational profile can be included in dynamic optimization, albeit with additional computational cost.
2) Using Eq. (32), time-dependent profiles for the failure probability are obtained using the strain over multiple cycles.
3) The failure probability over long-term operation is computed by assuming that each cycle is identical.

While producing the desired H_2 production rate, efficiency must be maximized and accumulation of residual thermal stress be minimized. For SOC, operating at high temperature improves the efficiency mainly due to reduced overpotential in the electrolyte while the high temperature operation and especially rapid temperature changes can adversely affect thermal stress. For this multi-objective dynamic optimization problem, the weighted sum method is used as given by Eq. (36).

$$\min_{\theta} \frac{1}{t_f} \int_0^{t_f} \left[P_{\text{system}}(t) + \sum_l \frac{1}{N_{x,l} N_z} \omega_l \sum_{iz=1}^{N_z} \sum_{ix=1}^{N_{x,l}} \left(\sigma_{l,iz,ix}(t) - \sigma^0_{l,iz,ix} \right)^2 \right] \mathrm{d}\, t \tag{26}$$

subject to:

$$h_{\text{sys}} \left(\xi, \frac{d\xi}{dt} \right) = 0 \tag{27}$$

$$h_{\text{deg}} \left(\sigma, \varepsilon, \xi, \frac{d\sigma}{dt}, \frac{d\varepsilon}{dt} \right) = 0 \tag{28}$$

$$\dot{m}_{H_2,0}(t) - \delta \leq \dot{m}_{H_2}(t) \leq \dot{m}_{H_2,0}(t) + \delta \tag{29}$$

$$\sigma_l^{\text{compressive,max}} \leq \sigma_{l,iz,ix}(t) \leq \sigma_l^{\text{tensile,max}} \tag{40}$$

$$\theta^{\text{lb}} \leq \theta \leq \theta^{\text{ub}} \tag{30}$$

$$\xi^{lb} \leq \xi(t) \leq \xi^{ub} \tag{31}$$

Here the objective function includes the following two terms: (i) the first term denotes the average power consumption over the cycle in MW (since the H_2 production rate is predetermined, this is equivalent to minimization of specific power consumption or maximization of efficiency) and (ii) the second term denotes the integral squared deviation of the stress distribution σ at a time t for all locations from the initial stress distribution σ^0in MPa. ω_l is a user-provided weight. Since the stress in each layer l can vary by several orders of magnitude, different values of ω_l can be assigned to each layer $l \in FE, E, OE$. The stress deviation at every point in time is averaged for the cell by dividing the summation with the number of x and z finite elements in each layer. Since each layer has a different thickness, different number of finite elements in the x direction can be used for every layer. h_{sys} is the system of equality constraints pertaining to the dynamic process model (SOEC and BOP equipment) with ξ and $\frac{d\xi}{dt}$ representing the system state variables and their respective derivatives. h_{deg} is the differential-algebraic equation (DAE) system derived from the thermal stress and creep deformation model described in Section 2.3. In Eq. (38), σ and ε are the degradation state variables for stress and strain, respectively, while $\frac{d\sigma}{dt}$ and $\frac{d\varepsilon}{dt}$ are their corresponding time derivatives. The constraint (Eq. 39) enforces the production profile described in Figure 4(a) by restricting the H_2 production rate at every point in time to the corresponding value from the predetermined cyclic operating profile within a tolerance δ. The constraint given by Eq. 40 provides bounds to the maximum allowable localized instantaneous compressive and tensile stresses during dynamic operation. The decision variables θ are bounded by lower and upper bounds based on reasonable operating regimes in Eq. 40.

Table 1 presents the baseline values and the bounds for the decision variables used for dynamic optimization. Here, we free the inlet temperatures to the SOC on the fuel and oxygen side and enforce lower and upper bounds.

Table 1. Base case values and bounds for the decision variables.

Decision variables θ	Unit	Base case (Min/Max H2 rate)	θ^{lb}	θ^{ub}
Steam heater outlet temperature setpoint	K	943.6/986.0	920	1000
Sweep heater outlet temperature setpoint	K	923.0/985.6	920	1000

2.7 Cell configuration and material properties

The SOC cell is considered to be fuel electrode-supported with Ni-YSZ as the fuel electrode, YSZ as the electrolyte, and LSM-YSZ as the oxygen electrode materials. The thicknesses of Ni-YSZ, YSZ, and LSM-YSZ layers are 1000 µm, 10.5 µm, and 40 µm, respectively. A single cell measures 23.45 mm in length.

The material property values for Young's modulus (E), Poisson's ratio (ν), coefficient of thermal expansion (CTE) (α), and creep parameters, A and N, of the cell components are shown in Table 2. Details on the uncertainty in these parameters can be found in the supplementary information in Figures S1 – S3 and Table S1.

Table 2. Material properties of SOEC materials

	Temperature (K)	Fuel electrode (Ni-YSZ)	Electrolyte (YSZ)	Oxygen electrode (LSM)
E (GPa)	1073	53	144	52
ν		0.39	0.29	0.28
α (10^{-6}/ K)		12.41	10.35	12.19
A ($MPa^{-n}s^{-1}$)		2.6×10^{-11}	1.18×10^{-14}	1.27×10^{-12}
N		1.7	1	1.7

The characteristic Weibull distribution parameters m, ε_0, and V_0 are different for each layer of the SOC structure and depend on the materials of construction (Table 3).

Table 3. Weibull parameters for SOC materials

Material of construction	m	ε_0	V_0
LSM-YSZ Oxygen Electrode	3.7	0.01	1.21
YSZ Electrolyte	8.6	0.01	0.35
NiO-YSZ Fuel Electrode	17.8	0.01	0.578

2.8 Modeling and optimization software

The dynamic process model for the SOEC flowsheet is developed by using the open-source, equation-oriented IDAES software framework [41], which is based on Pyomo, a Python-based open-source code. A comprehensive discussion of the plant-wide model and how the controller is configured can be found in Li *et al.* [37]. The Pyomo.DAE module is employed for the discretization of the time domain to transform the DAE into a system of nonlinear algebraic equations using the implicit Euler method.

The spatial variations within the cell are captured through finite-element discretization along the cell length. The flow direction is along the *z*-axis shown in Figure 1(a). The stress model is discretized over the x-direction with 16, 4, and 8 finite elements in the fuel electrode, electrolyte, and oxygen electrode, respectively. Note that these finite elements along the *x*-direction are only present in the stress model. The SOEC model uses a discretization strategy similar to Li *et al.* [37] with one finite element in each layer for the *x*-direction. The temperatures for the 28 finite elements in the stress model are obtained through interpolation from the SOEC temperature profile. Dynamic simulations are conducted using the adaptive timestep integrator PETSc [47] and served as the initial guess for the fully discretized optimization approach solved using IPOPT [48].

3. Results

3.1 Model validation

To validate the developed model we simulate the initial stress relaxation after the sintering of the SOC structure. Figure 2 shows excellent agreement between our model and results from Zhao *et al.* [17]under isothermal conditions (1073 K), accurately capturing the initial thermal stresses in the layers and interfaces of an SOFC [17], including when creep deformation occurs. We consider that the cell is sintered at a temperature of 1470 K. At this temperature the cell is considered to be at zero-stress and zero-strain. The cell temperature is brought to an operating temperature of 1073 K for operation. This results in the formation of the initial thermal stress profile described in Figure 2(a).Before stress gets fully relaxed, compressive stress develops in the electrolyte and oxygen-electrode layers due to the contraction of the fuel-electrode substrate. As illustrated in Figure 2(a), this results in a pronounced tensile stress peak near the fuel-electrode/electrolyte interface and considerable compressive stress within the electrolyte layer, measured at approximately 136.49 MPa. The difference in material properties including mismatch in coefficient of thermal expansion among the three layers results in the steep discontinuities in stress at the interfaces between the electrodes and the electrolyte.

Figure 2(b) and Figure 2(c) shows the evolution of total strain and stress, respectively, and compare these profiles with that from Zhao *et al.* [17]. Again, there is a good match between the proposed model with the reference. The total strain accumulation increases with time which leads to decreased stress and consequently a decrease in the creep rate.

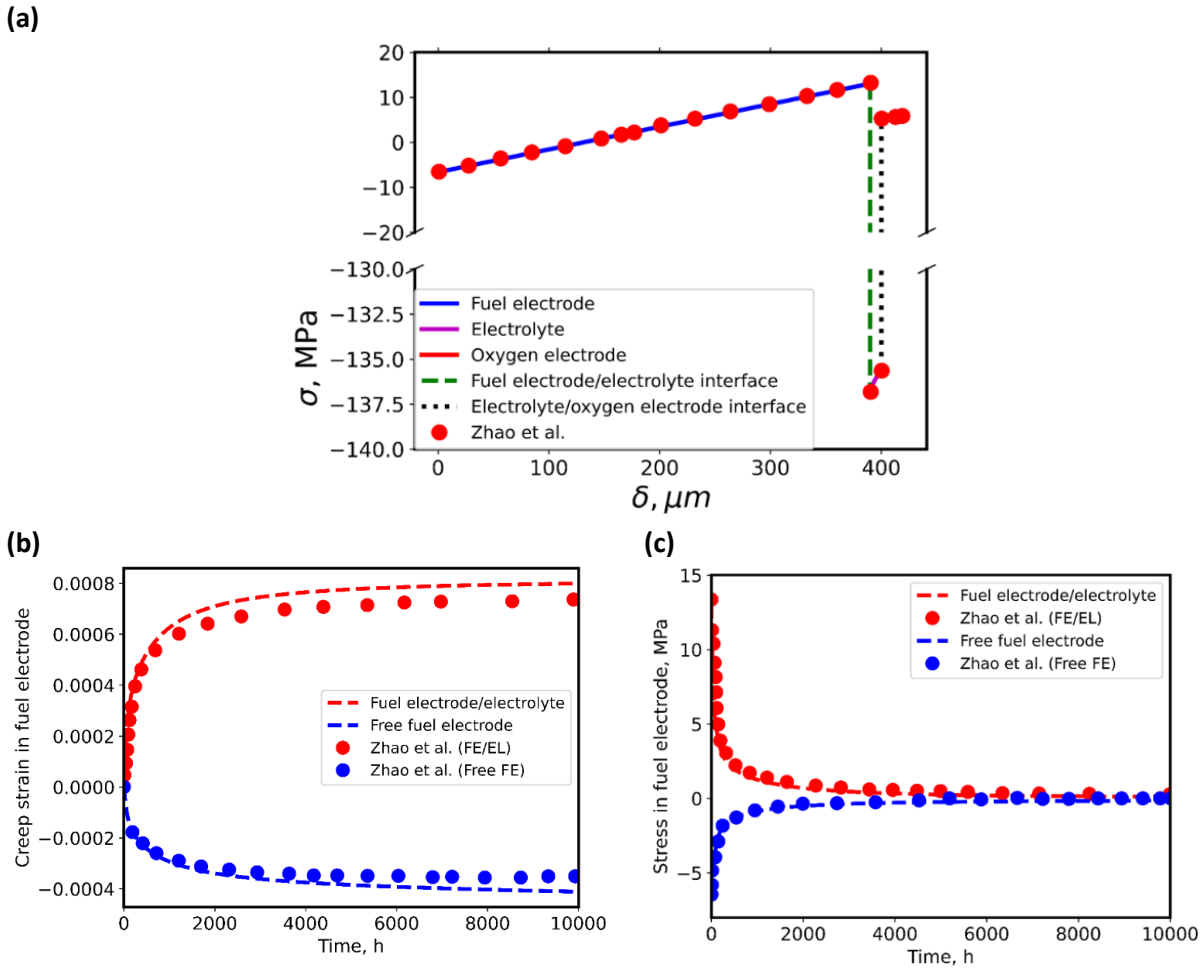

Figure 2. Validation with (Zhao et al., 2019) describing stress relaxation and creep deformation under isothermal conditions (1073 K).

3.2 Dynamic ramping simulations of the SOEC system

For the studies conducted in this and subsequent sections, initial condition (i.e., at t = 0) is considered to be when the cell is stress-free (i.e., post stress relaxation as observed in the study presented in the earlier section) but it has non-zero creep strain due to the deviation of the initial temperature compared to the sintering temperature during manufacturing. The steady-state targets for dynamic simulation are determined by solving an optimization problem that minimizes the total electricity usage of the cell and

associated BOP equipment. Similar to Li *et al.* [37], steady-state setpoints are optimized by solving individual steady-state optimization problems for fixed H_2 production rates. These setpoint variables include cell potential, makeup steam/hydrogen feed rate, sweep feed rate, and temperature setpoints for steam and sweep heater outlets. Note, that during dynamic optimization the only free variables are the temperature setpoints of the steam and sweep heaters as discussed in Table 1. This section of the paper will first show the impact of a classical control strategy for a single cycle of H_2 production changes on cell temperature, a key parameter the impacts stress, and then the subsequent impact of multiple H_2 cycles on the stress accumulation. More importantly, it demonstrates how a stress penalty can be added to the nonlinear model predictive control (NMPC) objective to mitigate stress accumulation.

In order to study the effects of different load cycles on the stress distribution in the SOC structure, the following case study was conducted. We simulate three duty cycles, each consisting of initial operation at a maximum H2 production rate of 2.0 kg/s followed by a 5-minute ramp down to a low H2 production rate which is maintained for 5 hours, before finally ramping back up to 2.0 kg/s over the course of 5 minutes which is held for an additional two hours. The three cases differ in the values of the minimum H2 production rate at the end of ramp down, that are 0.4 kg/s, 1.0 kg/s and 1.5 kg/s, respectively. The system level setpoints for each of these H2 production targets (including the starting 2.0 kg/s) are obtained through the solution of a separate steady state optimization problem as discussed in a previous work[49].

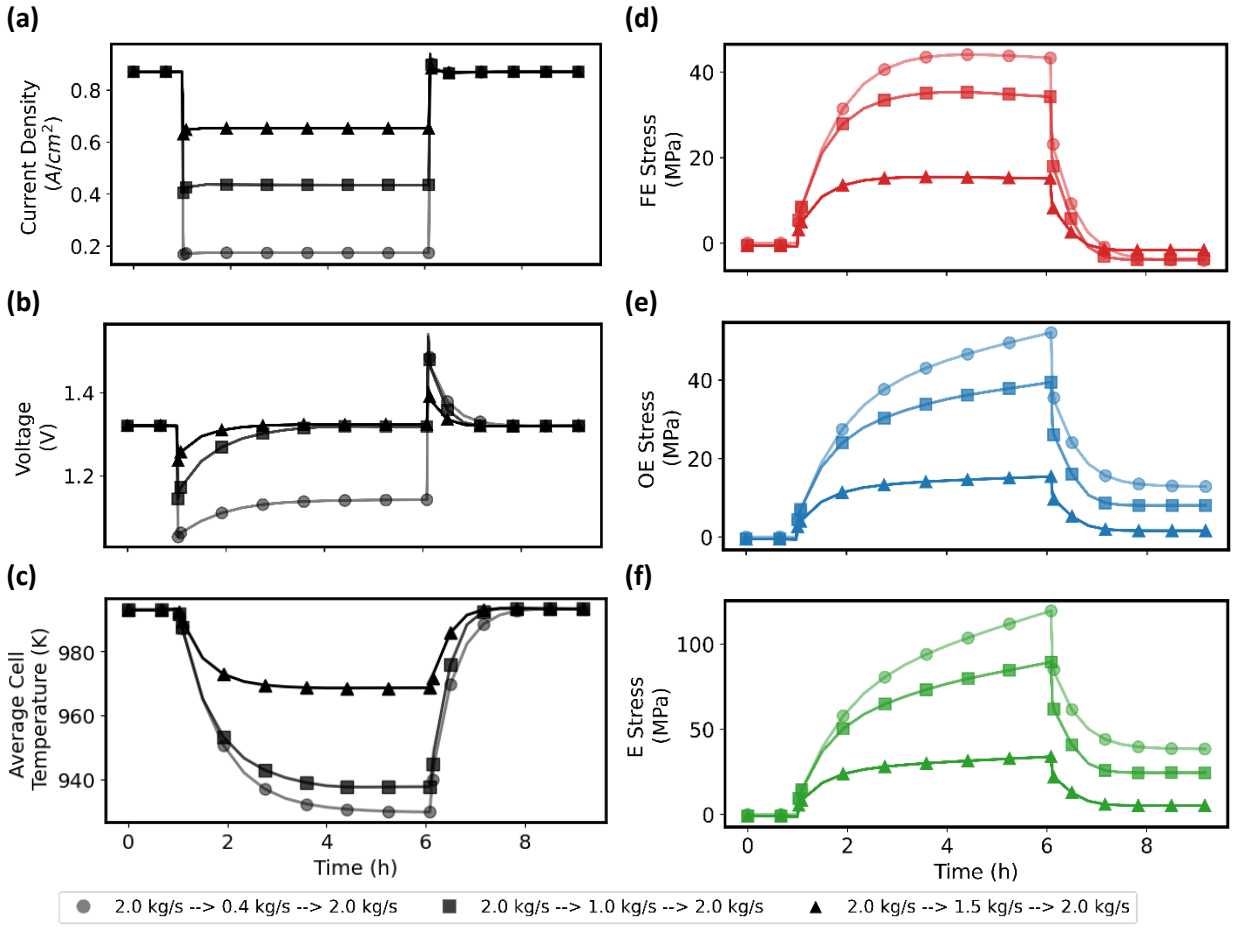

Figure 3 Single cycle stress redistribution compared to three ramping cases. (a-c) Operating conditions for the ramp. (d-f) Stress evolution over a single cycle

Figure 3(a) presents the variation in current density over the 9-hour operating period due to the desired change in the hydrogen production rate. The corresponding voltage profiles are shown in Figure 3(b). Notably, the resulting voltage for achieving the 0.4 kg/s H2 production setpoint is approximately 1.14 V, which is below the thermoneutral voltage (TNV), whereas the voltages for other production rate set points remain above TNV. The stack operating temperature changes accordingly, as the stack transitions from/to the exothermic mode (above TNV) to/from the endothermic mode (below TNV) as seen in Figure 3 (c). Therefore, as expected, average cell temperature is highest corresponding to 2.0 kg/s H2 production rate, followed by 1.5 kg/s and 1.0 kg/s H2 production rate, with the lowest average temperature observed for the 0.4 kg/s H2 production rate.

A notable peak in stress is observed towards the end of the ramp down period as stack temperatures drop. As seen in Figure 3(d-f), the highest stresses are observed in the electrolyte, peaking at about 130 MPa for 0.4 kg/s H2 production rate. It is observed that there is a strong dependance of stress on the difference between the operating temperature and the sintering (zero-stress) temperature as expected. In addition,

it is observed that the operating cycles that include a transition from above the TNV to below the TNV yield higher thermal stress than where such transition is avoided.

Therefore, from this point this study focusses on the load schedule as described in Figure 4(a). The cell starts the cycle operating at a H_2 production rate of 2.0 kg/s, followed by a ramp decrease to 0.4 kg/s over a period of 5 minutes, which is then maintained for 5 hours. Next, the production rate increases back up to 2.0 kg/s over 5 minutes and is held constant for an additional 2 hours. It should be noted that the H_2 flowrate rate of 2 kg/s leads to exothermic operation while the lower H_2 flowrate of 0.4 kg/s leads to endothermic operation. It is desired to study the optimal profile as electrolysis operation swings from above to below the thermo-neutral voltage of 1.29 V and vice versa as shown in Figure 4(b).

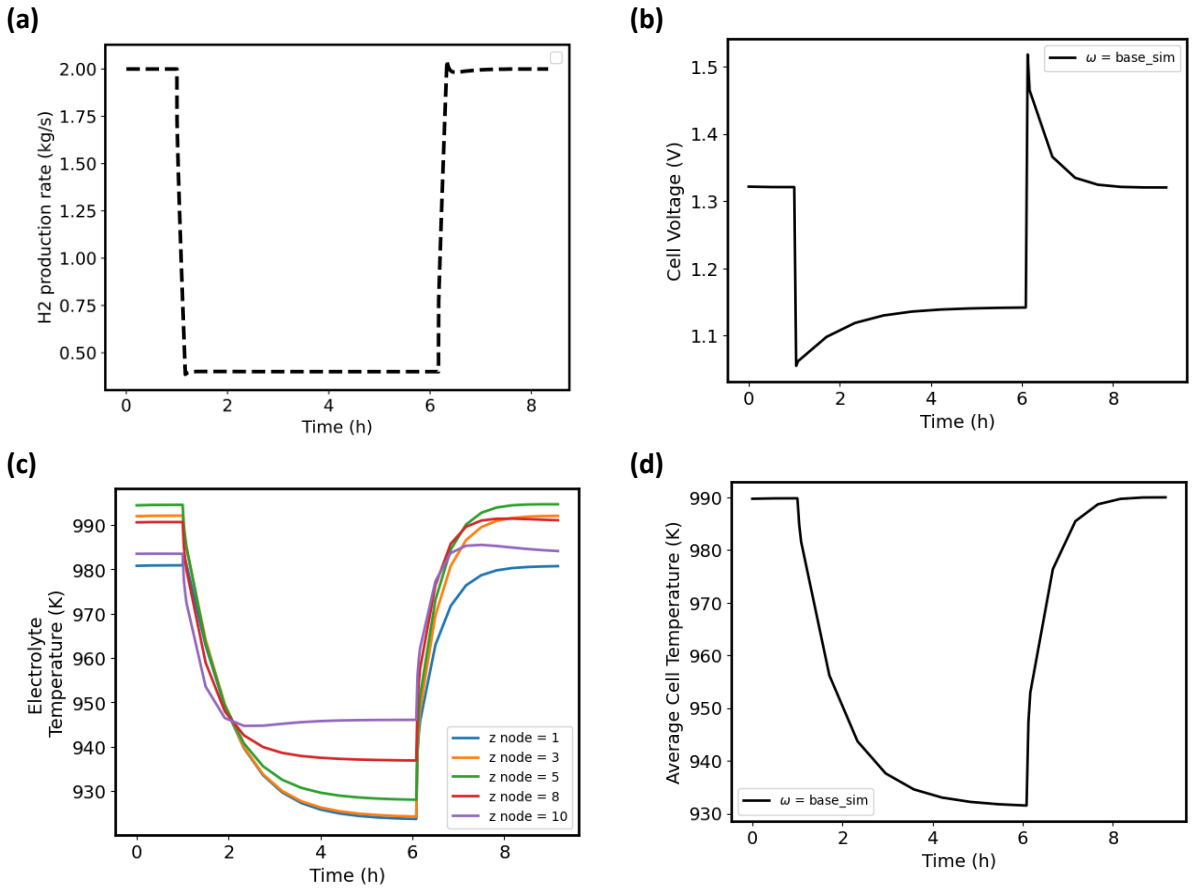

Figure 4. (a) H_2 production rate, (b) cell voltage, (c) electrolyte temperature profiles at different locations along the cell length and (d) average temperature at the center of the cell

Figure 4(c) shows the stack core temperature profile over the course of the cycle at different locations (nodes 1 to 10) along the length of cell (*z*-direction). The spatio-temporal variation in the temperature profile indicates expected variation in the stress profile. Interestingly, it is observed that at high H_2 production rates, the highest temperatures occur near the center of the stack. However, at low production rates, the highest temperature region shifts towards the fuel outlet due to endothermic operation. Higher thermal stress results as the difference in the operating temperature increases from the zero-stress condition. For conciseness, Figure 4(d) shows the average cell temperature over the course of dynamic operation.

3.3 Stress reduction through dynamic optimization

As a base case, we evaluate the stress and strain distribution corresponding to the temperature profile in Figure 4(c-d) over five identical cycles. Figure 5 show the stress and strain evolution in each layer at the location of maximum tensile stress, specifically at the interface between the fuel electrode and the electrolyte. At the start of the cycles (t=0 hours), the stress in all three layers is zero, consistent with the stress relaxation described in Figure 2. Correspondingly, the initial strain in all locations across the three layers is non-zero. Figure 5 also presents stress and strain profiles for varying values of the penalty parameter ω (i.e., the weight in the multi-objective optimization problem) used in the electricity minimization objective function described in Eq. (36). The dynamic optimization results demonstrate that increasing the value of the penalty value reduces stress but comes at the expense of higher electricity consumption for achieving the desired hydrogen production. The impact of applying dynamic optimization to decrease residual stress will be discussed in more detail below.

Figure 5(a) shows the stress evolution in the fuel electrode specifically near the fuel-electrode – electrolyte interface. It is observed that as the cell transitions from a high H_2 production rate to a low H_2 production rate, without accounting for stress mitigation, the shift to endothermic operation causes a temperature decrease. This results in a considerable increase in the tensile stress in the fuel electrode, reaching approximately 40 MPa (black line). This is accompanied by an increase in the creep strain seen in Figure 5(b). As the cell ramps back up to 2.0 kg/s, cell temperatures increase back to the initial 990 K. While the stress due to thermal mismatch is relieved along with the increase in temperature, residual stress relaxation through the creep deformation process has resulted in the accumulation of creep strain. Furthermore, the stress accumulated is not completely relaxed within the cycle time resulting in a non-zero residual strain at the end of the first cycle.

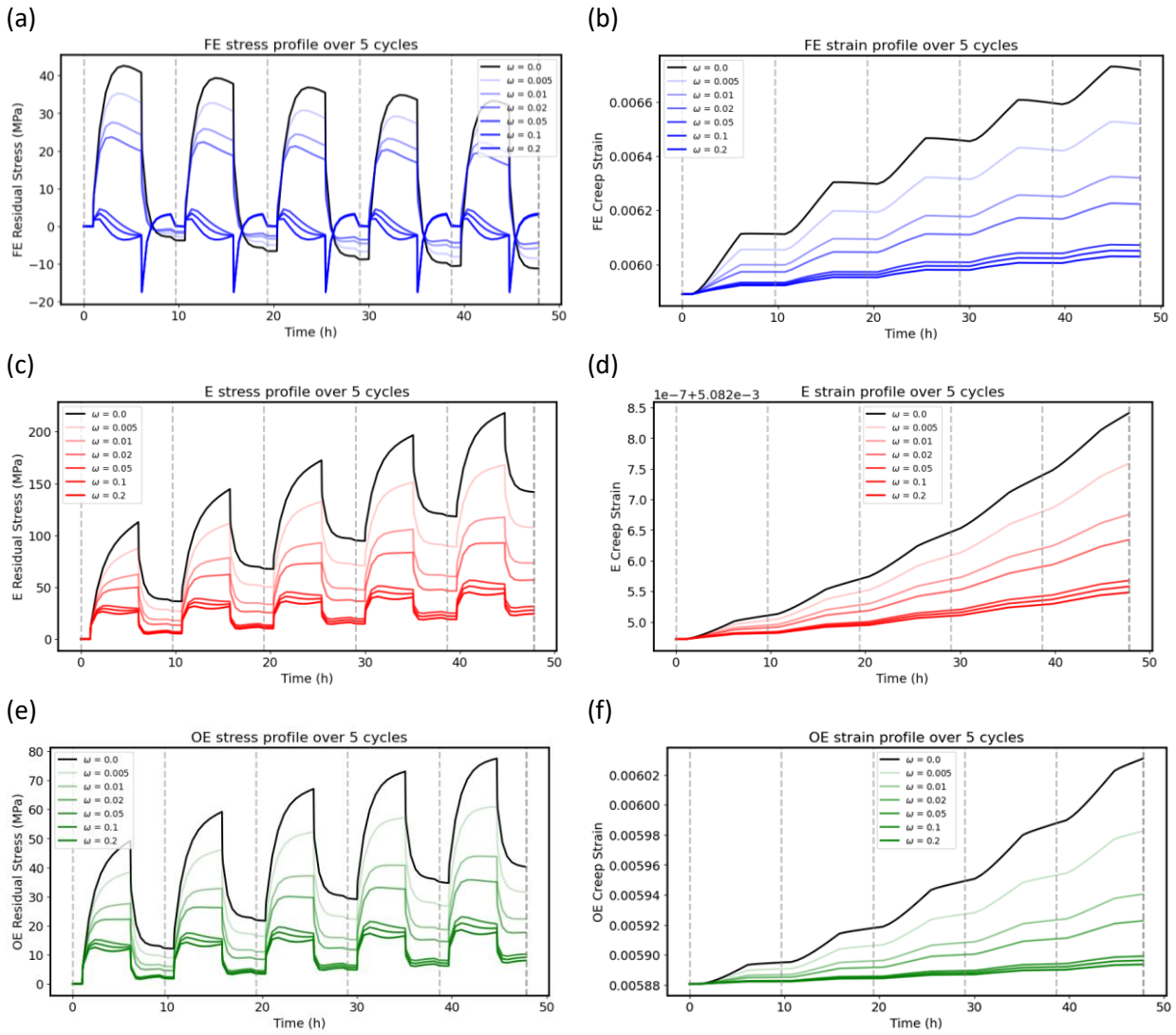

Figure 5. Stress and Strain evolution over 5 operating cycles in Fuel Electrode (a-b), Electrolyte (c-d) and Oxygen Electrode (e-f). $\omega = 0$, corresponds to the base case and $\omega = 0.2$ includes a stress penalty with the highest penalty.

This effect is very evident in the results for the electrolyte and oxygen electrode, as shown in Figure 5(e) and Figure 5(f), respectively. In these cases, the starting stress at the beginning of each new cycle is higher than that of the previous cycle. The electrolyte material (YSZ) is generally very resilient to high stress conditions due to a small creep rate constant ($A=1.18 \times 10^{-14}$ $MPa^{-n}s^{-1}$) resulting in low strain deformation over the 50 hours of operation even under high tensile stresses.

As described in Figure 5(e-f) the oxygen electrode experiences moderately high tensile stress (~50 MPa during the first cycle), which accumulate to exceed 75 MPa over the course of just five cycles. This leads to a steeply increasing strain profile, which is likely to cause accelerated damage and premature failure if not addressed. Thus, while dynamic operating scenarios designed to maximize efficiency and reduce

energy costs may achieve short-term savings, they can ultimately lead to higher capital costs due to the need for frequent stack replacements.

In the base case (ω = 0), we also observe significant spatial variations in thermal stress in both the compressive and tensile directions. Figure 6(a) represents spatial stress distribution as a 2D heatmap in which the red regions experience tensile stress, and the blue regions experience compressive stress. The white region represents the interface between regions of compressive and tensile stress, characterized by near zero stress levels. Figure 6(b) illustrates the stress distribution in the SOEC at the end of the final cycle before the ramp up back up to a H_2 production rate of 2.0 kg/s. This corresponds to the maximum stress observed in the cell over the five cycles. It is observed here that the entire cell experiences tensile stress, with the maximum stress occurring at the interface between the electrolyte and the fuel electrode.

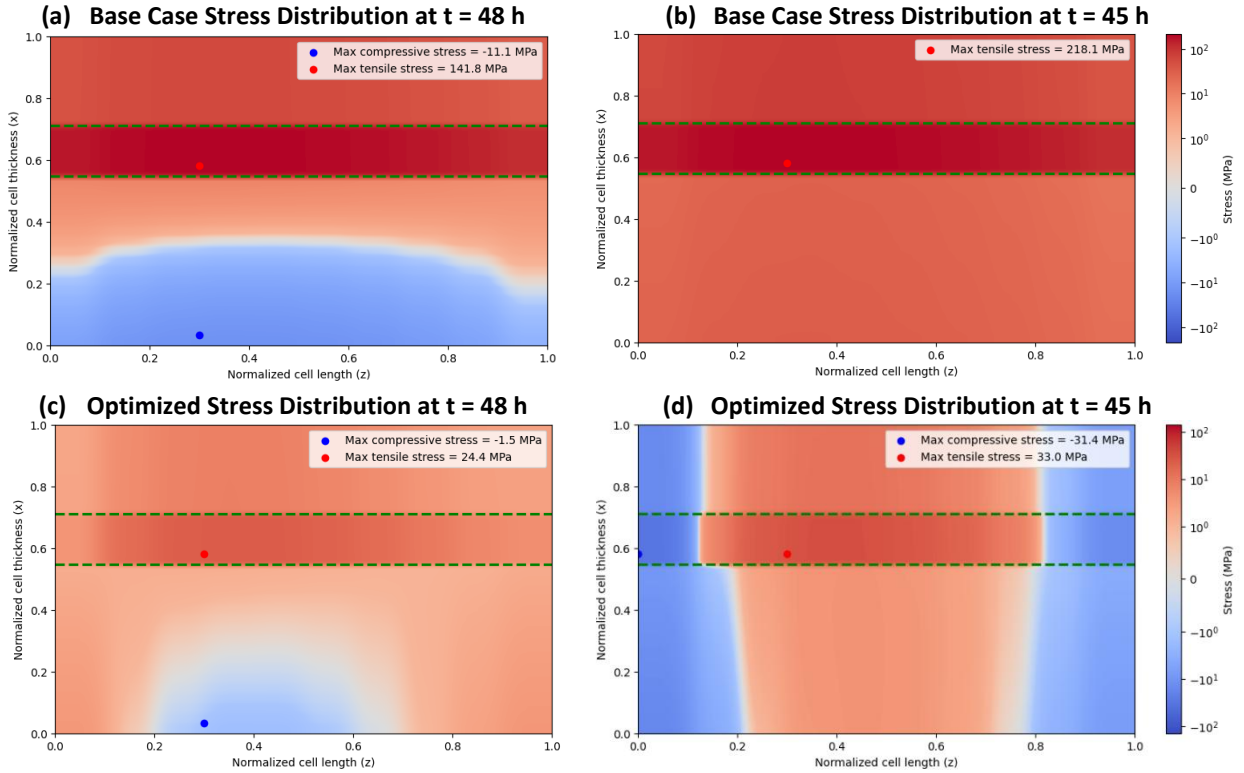

Figure 6. Spatial Stress Distribution at time = 48 hours and time = 45 hours for the base case (a-b) and the optimized (ω = 0.2) case (c-d)

As noted above, in Figure 5 we also plot operating trajectories for increasing values of the penalty parameter, corresponding to stress accumulation in the objective function specified in Eq. (36). The dynamic optimization results show that increasing the value of the penalty parameter is effective in decreasing residual stress in all three layers by up to 80%, 85%, and 87% in the oxygen electrode, electrolyte, and fuel electrode, respectively. Figure 7 shows the corresponding temperature and voltage trajectories required to achieve these stress reductions for each value of ω. Optimization reduces the maximal stress by increasing the average cell temperatures during the low H_2 production phase of 0.4 kg/s. For the oxygen electrode and electrolyte, this results in a monotonic decrease in stress, which significantly mitigates the increase in strain. In the fuel electrode (Figure 5(a)), the peak tensile stresses initially decrease monotonically for low values of the penalty weight ω. However, at higher penalty weights, the reduction in tensile stress is accompanied by a significant spike in compressive stress before the ramp up

to a H_2 production rate of 2.0 kg/s. It is noted that fuel electrode and oxygen electrode materials exhibit high resistance to compressive stress and are not expected to fail under these stresses. At the end of five cycles, the maximum compressive stress, approximately -11.1 MPa, is observed near the fuel electrode–interconnect interface. The maximum tensile stress is observed at the interface between the electrolyte and fuel electrode.

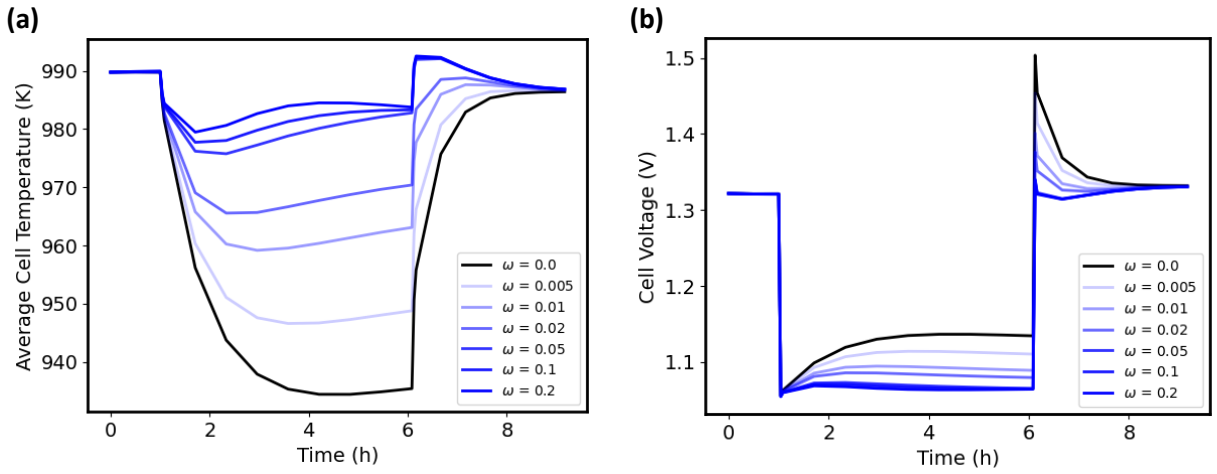

Figure 7. Optimal cell (a) temperature and (b) voltage for different stress penalty weights

The spatial temperature profiles after optimization including the highest stress penalty are seen in Figure 6. From Figure 6(c), it is observed that the stress at the final-end state is significantly reduced, with an 82% decrease in the maximum tensile stress to 24.4 MPa, along with a similar reduction in the tensile stress. At 45 hours, corresponding to the point of maximum stress in the base case, an 84% reduction in tensile stress is observed at the electrolyte-fuel electrode interface. However, this reduction comes at the expense of an increased presence of compressive stress along all three layers of the SOEC. These stresses are concentrated near the cell's inlet and outlet, with a maximum compressive stress of -31.4 MPa observed at the fuel electrode-electrolyte interface near the fuel inlet. This value approaches the allowable tensile stress limit for the electrolyte (-30 MPa).

3.4 Quantification of material property uncertainty

As discussed in the section on parametric uncertainty in SOEC material properties, there is considerable uncertainty in the Young's modulus, the coefficient of thermal expansion, and Poisson's ratio. In Figure 8, these uncertainties are propagated by simulating the $\omega = 0.2$ optimal operating profiles under different realizations of uncertainty. "Base case" here corresponds to the stress profiles obtained from the expected value of the parameters. The "Full space" is bounded by lower and upper bound realizations of all the parameters. Because of the nature of the stress models, these correspond to the worst-and best-case conditions. We also construct 95% confidence intervals using the data described in the supplementary information. The regions marked "95% confidence" are obtained from the lower and upper bounds of this reduced uncertainty space. It is seen in Figure 8(a), Figure 8(c) and Figure 8(e) that the uncertainty in the

parameters results in a significant uncertainty in the stress evolution in the three SOEC layers, with higher levels of uncertainty when projecting over longer operating horizons. The largest uncertainties are observed in the oxygen electrode.

The growing uncertainty in evolution of stress over time further implies significant uncertainty in the failure probability estimates throughout the five cycles. The failure probability evolution over five cycles is presented for $\omega = 0.2$ in Figure 8(b), Figure 8(d) and Figure 8(f). We observe that the oxygen electrode and fuel electrode have a much higher probability of creep induced failure compared to the electrolyte. As mentioned earlier, the maximum instantaneous compressive and tensile stresses are constrained through inequalities. These constraints, in conjunction with the stress penalty, lead to a decrease in the transient spike in stress observed at the end of the ramp, resulting in a flatter stress profile before the ramp up to 2.0 kg/s. The fuel electrode exhibits an interesting property of elastic SOEC materials, since some of the creep strain can be reversed, thereby reducing failure probability, when the stress transitions from tensile to compressive. In these operating profiles, the duration of reversal is much shorter than the duration of the period in which the cell is under compressive stress. However, this could motivate the development of specialized operating schedules where the stack undergoes a “regenerative” period where strain could either be reversed or the residual stresses could be relieved through the relaxation process. The latter can be achieved by extended isothermal operation like that in Figure 2.

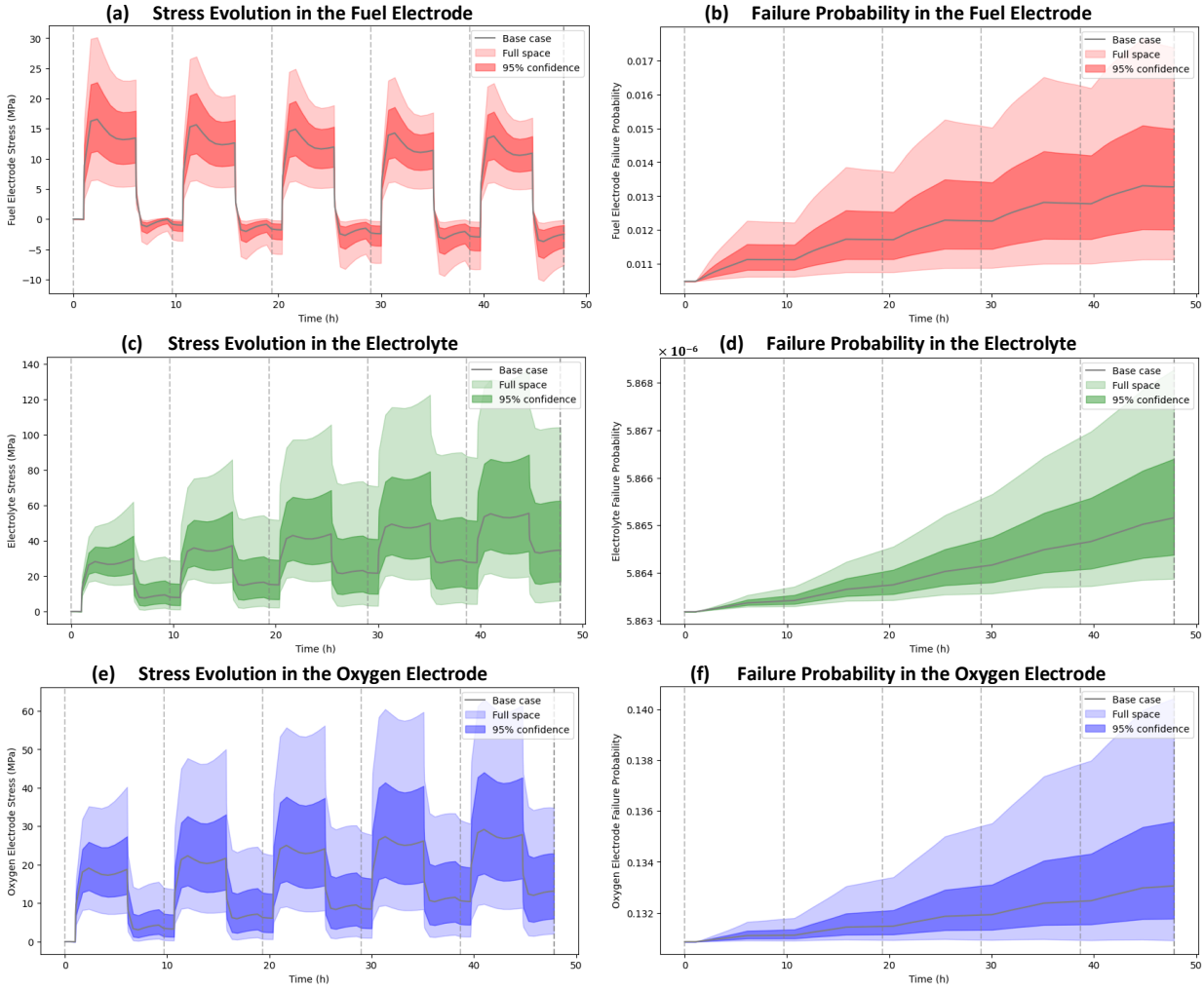

Figure 8. Effect of material property uncertainties on residual stress evolution and failure probability in the Fuel Electrode (a-b), Electrolyte (c-d) and Oxygen Electrode (e-f)

The stress reduction strategies described in the previous sections have an impact on the energy consumption of the SOEC-based hydrogen generation process. Increasing the cell temperatures during low-load conditions (0.4 kg/s H_2) incurs a higher energy cost, as the cell operates endothermically during this period. Figure 9 presents a Pareto plot that indirectly compares the two competing objectives of annual energy consumption and estimated time to stack replacement as defined in Section 2.4. Under rapid cycling operation, as described in this study, stress accumulation is exacerbated by the slow dynamics of the residual stress. This leads to accelerated creep deformation, ultimately resulting in a shortened cell lifespan. Since the stack should be replaced well before failure is imminent, a failure probability of 60% is assumed as the threshold for replacement as noted before. As shown in Figure 9, while dynamic optimization can extend the replacement time, it results in an increase in the annual energy consumption due to the trade-off with efficiency. The limiting component for stack replacement is the oxygen electrode. Depending on the method of operation, stack replacement times can range from three months to six years,

while energy consumption can vary from $47.5\ \mathrm{kWh\ /kg\ H_2}$ to $50.5\ \mathrm{kWh\ /kg\ H_2}$. The Pareto curve offers a set of operating points that shows the tradeoff between the two objectives. It shows that if it is desired to increase the stack replacement time, it leads to steeper energy penalty.

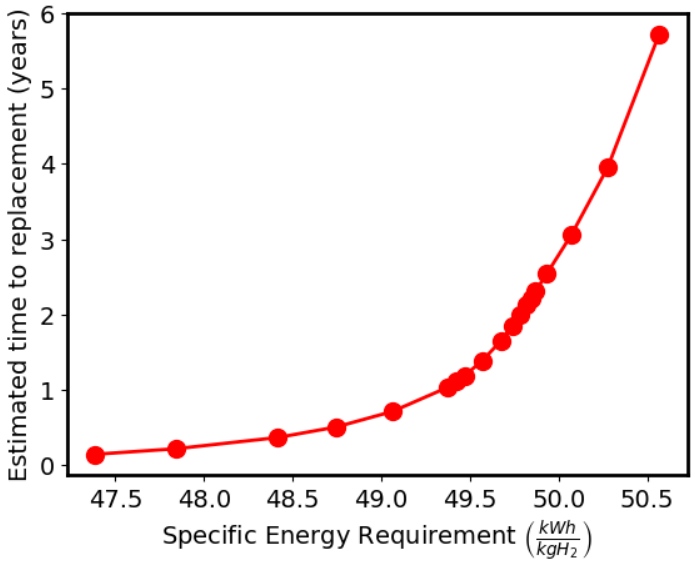

Figure 9. Pareto-curve comparing specific energy consumption and expected time to replacement.

The Pareto curve can be used to obtain the optimal operating conditions given the cost of energy and stack. However, these prices greatly vary based on the specific region/location. Our prior related studies on long-term chemical degradation of SOEC systems have shown that the trade-off between short-term efficiency and long-term replacement costs is highly market dependent[32,34]. For example, in regions with high electricity prices, operating profiles that favor efficiency—despite more frequent replacements—tend to minimize the long-term levelized cost of hydrogen. Conversely, in markets with lower electricity costs, reduced efficiency and longer stack lifetime may be more economic.

4. Conclusion

While load-following cyclic operation is an attractive application for SOEC systems due to their fast thermal and electrochemical dynamics, this study shows that, without careful optimization of dynamic operation, rapid stress build-up and resultant deformation can significantly shorten stack lifetime. The dynamic stress and creep deformation model presented here serves as a crucial tool to understand the physical degradation of SOEC stacks, especially in the absence of experimental methods for monitoring cell deformation during operation.

The model captures the dynamics of the multi-timescale deformation process by accounting for both the instantaneous stress formation caused by thermal mismatch and the much slower creep deformation process. Implemented within the open-source IDAES framework, this deformation model can be readily coupled with the publicly available SOEC system model.

Simulation results show significant variations in the stress magnitudes and directions throughout the cell, with both compressive and tensile stresses present in different layers of the SOEC. These stress distributions are time dependent and heavily influenced by the operating conditions during dynamic operation. While stresses caused by thermal mismatches are instantaneous and follow the temperature dynamics, they contribute to a slower creep deformation process.

Even though the stresses developed during transient operation are reduced by returning to the initial zero-stress temperature, the residual stress does not completely relax within the cycle. This results in a compounding effect, where the initial stress at the start of each subsequent cycle is higher than the previous one. Over long-term operation, this accumulation of stress can ultimately lead to stack failure.

Dynamic optimization is shown to be effective in controlling physical degradation and increasing the stack lifetime, from a base case of three months to over six years, based on the assumption that the stack must be replaced when the failure probability exceeds 60%. This highlights the importance of considering both physical degradation and efficiency when dynamically operating the stack.

Although dynamic optimization leads to a reduction in physical degradation through multiple mechanisms, including slow creep deformation and instantaneous thermal stress, by using stress constraints and a penalty function, it leads to a decrease in the efficiency. A Pareto curve is generated showing the stack replacement time and specific energy requirement. It shows that if the stack replacement time is desired to be higher than about one year, then the energy penalty steeply increases. For example, if the stack would be replaced in 0.5 yr, specific energy requirement would be 48.5 kWh/kg H_2 while for a stack replacement time of about 6 yr, the specific energy requirement rises by about 4.2%. Obviously, the optimal operating conditions for cyclic operation will depend on the capital cost of the stack, energy cost, and market incentives for cyclic load-following operation. The optimal condition selected based on the Pareto-front is highly dependent on the specific region/location under consideration. Furthermore, it is important to consider the real-time economics of electricity prices and hydrogen demand. Additionally, other strategies to mitigate stress evolution may include scheduling restorative periods during long-term operations, where the cell operates isothermally to allow built-up stresses to relax. Incorporating such long-term scheduling decisions into the day-to-day dynamics of thermal stress requires multi-timescale optimization models, which can be computationally expensive. The multi-objective optimization problem proposed in this work and other variants of it including the scenarios and operational strategies as noted above can lead to a highly computationally expensive dynamic optimization problem especially for large-scale industrial systems. For computational tractability of these problems, in addition to selection/development of efficient optimization algorithms and strategies, other strategies should be investigated including simplified/reduced model of the stack and balance of the process, reduction of the scenario space, potential use of parallel computing, etc.

While the theoretical approach developed in this work can be applied to other ceramic materials used in SOECs, we recognize that there is a high degree of uncertainty in the structural parameters of the SOEC materials. Monte Carlo simulations undertaken in this work show that the stress-induced failure probability and uncertainty in the failure probability are considerably higher for the fuel and oxygen electrodes compared to the electrolyte. The oxygen electrode exhibits about 10 times higher failure probability compared to the fuel electrode. To address materials uncertainties, future work could explore robust optimization techniques to obtain operating profiles capable of maintaining feasibility under all realizations of uncertainty.

This work models the cell as a multi-layer structure with uniform material properties for each component described by macroscopic structural properties such as the coefficient of thermal expansion, Poisson's ratio, and the Young's modulus. Characterization at the microstructure level by taking into account local inhomogeneities and microscale mechanisms, such as grain boundary sliding, local creep at heterogeneities, microcrack formation, and localized contact resistances are not taken into account in the current work. Accounting for these effects would require high-fidelity multiphysics models that are computationally prohibitive for dynamic optimization. In addition, there is a lack of literature on detailed theoretical studies quantifying these phenomena and measurement of local thermo-mechanical properties with well-defined local inhomogeneities further limiting their integration into system-level models. It is desired that future works in this area address these important aspects.

Finally, it is important to recognize that in addition to failure due to thermal stress and creep deformation, a significant challenge towards the commercialization of high temperature SOC stacks is that of performance degradation due to a variety of chemical degradation mechanisms. These include phase coarsening, TPB degradation and the formation of secondary oxide scales that often work synergistically to reduce the useable lifetime of the SOC stack. It is highly desired that future works in this area account for these synergistic interactions to optimize operational profiles for long-term operation of the SOC systems.

AUTHOR INFORMATION

Corresponding Author

*Tel:1-304-293-9335, E-mail: Debangsu.Bhattacharyya@mail.wvu.edu

CRediT Authorship Contribution Statement

Nishant V. Giridhar: Conceptualization, Methodology, Software, Writing – Original Draft,

Quang Minh Le: Conceptualization, Methodology, Software, Writing – Original Draft,

Douglas A. Allan: Software, Project Administration,

Eric Liese: Writing – Review & Editing, Project Administration.

Stephen E. Zitney: Writing – Review & Editing, Project Administration.

Debangsu Bhattacharyya: Conceptualization, Methodology, Supervision, Writing – Review & Editing, Funding Acquisition.

Declaration of Competing Interest

The authors declare that they have no known competing financial interests or personal relationships that could have appeared to influence the work reported in this paper.

Acknowledgments

This work was conducted as part of the Institute for the Design of Advanced Energy Systems (IDAES) with support from the U.S. Department of Energy's Office of Fossil Energy and Carbon Management (FECM) through the Simulation-based Engineering Research Program.

Disclaimer

References

(1) Naeini, M.; Cotton, J. S.; Adams, T. A. An Eco-Technoeconomic Analysis of Hydrogen Production Using Solid Oxide Electrolysis Cells That Accounts for Long-Term Degradation. *Frontiers in Energy Research* **2022**, *10*.

(2) Yang, C.; Guo, R.; Jing, X.; Li, P.; Yuan, J.; Wu, Y. Degradation Mechanism and Modeling Study on Reversible Solid Oxide Cell in Dual-Mode — A Review. *International Journal of Hydrogen Energy* **2022**, *47* (89), 37895–37928. https://doi.org/10.1016/j.ijhydene.2022.08.240.

(3) Chiang, L. K.; Liu, H. C.; Shiu, Y. H.; Lee, C. H.; Lee, R. Y. Thermo-Electrochemical and Thermal Stress Analysis for an Anode-Supported SOFC Cell. *Renewable Energy* **2008**. https://doi.org/10.1016/j.renene.2008.02.023.

(4) Peng, J.; Huang, J.; Wu, X. long; Xu, Y. wu; Chen, H.; Li, X. Solid Oxide Fuel Cell (SOFC) Performance Evaluation, Fault Diagnosis and Health Control: A Review. *Journal of Power Sources*. 2021. https://doi.org/10.1016/j.jpowsour.2021.230058.

(5) Liu, L.; Kim, G.-Y.; Chandra, A. Modeling of Thermal Stresses and Lifetime Prediction of Planar Solid Oxide Fuel Cell under Thermal Cycling Conditions. *Journal of Power Sources* **2010**, *195* (8), 2310–2318. https://doi.org/10.1016/j.jpowsour.2009.10.064.

(6) Eichhorn Colombo, K. W.; Kharton, V. V; Berto, F.; Paltrinieri, N. Mathematical Modeling and Simulation of Hydrogen-Fueled Solid Oxide Fuel Cell System for Micro-Grid Applications - Effect of Failure and Degradation on Transient Performance. *Energy* **2020**, *202*, 117752. https://doi.org/10.1016/j.energy.2020.117752.

(7) Xu, Q.; Guo, M.; Xia, L.; Li, Z.; He, Q.; Zhao, D.; Zheng, K.; Ni, M. Temperature Gradient Analyses of a Tubular Solid Oxide Fuel Cell Fueled by Methanol. *Transactions of Tianjin University* **2022**. https://doi.org/10.1007/s12209-022-00331-0.

(8) Nakajo, A.; Stiller, C.; Härkegård, G.; Bolland, O. Modeling of Thermal Stresses and Probability of Survival of Tubular SOFC. *Journal of Power Sources* **2006**, *158* (1), 287–294. https://doi.org/10.1016/j.jpowsour.2005.09.004.
(9) Greco, F.; Frandsen, H. L.; Nakajo, A.; Madsen, M. F.; Van herle, J. Modelling the Impact of Creep on the Probability of Failure of a Solid Oxide Fuel Cell Stack. *Journal of the European Ceramic Society* **2014**, *34* (11), 2695–2704. https://doi.org/10.1016/j.jeurceramsoc.2013.12.055.
(10) Greco, F.; Nakajo, A.; Wuillemin, Z.; Van herle, J. Thermo-Mechanical Reliability of SOFC Stacks during Combined Long-Term Operation and Thermal Cycling. *ECS Transactions* **2015**, *68* (1), 1921. https://doi.org/10.1149/06801.1921ecst.
(11) Peksen, M. 3D CFD/FEM Analysis of Thermomechanical Long-Term Behaviour in SOFCs: Furnace Operation with Different Fuel Gases. *International Journal of Hydrogen Energy* **2015**, *40* (36), 12362–12369. https://doi.org/10.1016/j.ijhydene.2015.07.018.
(12) Wang, Y.; Jiang, W.; Song, M.; Zhang, Y.; Tu, S.-T. Effect of Frame Material on the Creep of Solid Oxide Fuel Cell. *International Journal of Hydrogen Energy* **2019**, *44* (36), 20323–20335. https://doi.org/10.1016/j.ijhydene.2019.05.220.
(13) Guo, M.; Lin, Z. Long-Term Evolution of Mechanical Performance of Solid Oxide Fuel Cell Stack and the Underlying Mechanism. *International Journal of Hydrogen Energy* **2021**, *46* (47), 24293–24304. https://doi.org/10.1016/j.ijhydene.2021.04.196.
(14) Luo, Y.; Jiang, W.; Zhang, Q.; Zhang, W. Y.; Hao, M. Effects of Anode Porosity on Thermal Stress and Failure Probability of Planar Solid Oxide Fuel Cell with Bonded Compliant Seal. *International Journal of Hydrogen Energy* **2016**, *41* (18), 7464–7474. https://doi.org/10.1016/j.ijhydene.2016.03.117.
(15) Zhang, Y.-C.; Lu, M.-J.; Jiang, W.; Tu, S.-T.; Zhang, X.-C. Effect of the Geometrical Size on Time Dependent Failure Probability of the Solid Oxide Fuel Cell. *International Journal of Hydrogen Energy* **2019**, *44* (21), 11033–11046. https://doi.org/10.1016/j.ijhydene.2019.02.155.
(16) Sun, Y.; Hu, X.; Gao, J.; Han, Y.; Sun, A.; Zheng, N.; Shuai, W.; Xiao, G.; Guo, M.; Ni, M.; Xu, H. Solid Oxide Electrolysis Cell under Real Fluctuating Power Supply with a Focus on Thermal Stress Analysis. *Energy* **2022**, *261*, 125096. https://doi.org/10.1016/j.energy.2022.125096.
(17) Zhao, X.; Lu, Y.; Song, X.; Wang, F. Evolution of the Residual Stress in Solid Oxide Fuel Cell during Creep. *J Aust Ceram Soc* **2019**, *55* (3), 681–687. https://doi.org/10.1007/s41779-018-0277-1.
(18) Colombo, K. W. E., K. W.; Kharton, V. V.; Berto, F.; Paltrinieri, N. Transient System-Level Performance and Thermo-Mechanical Stress Analysis of a Solid Oxide Fuel Cell-Based Power Generation Plant with a Multi-Physics Approach. *Computers and Chemical Engineering* **2020**. https://doi.org/10.1016/j.compchemeng.2020.106972.
(19) Colombo, K. W. E.; Kharton, V. V.; Berto, F.; Paltrinieri, N. Mathematical Multi-Physics Modeling and Simulation of a Solid Oxide Fuel Cell Unit for Thermo-Mechanical Stress Analyses. *Journal of The Electrochemical Society* **2020**. https://doi.org/10.1149/1945-7111/ab75fb.
(20) Colombo, K. W. E.; Kharton, V. V. Start-Up of a Solid Oxide Fuel Cell System with a View to Materials Science-Related Aspects, Control and Thermo-Mechanical Stresses. *Crystals* **2021**, *11* (7). https://doi.org/10.3390/cryst11070732.
(21) Liang, Z.; Wang, J.; Ren, K.; Jiao, Z.; Ni, M.; An, L.; Wang, Y.; Yang, J.; Li, M. Discovering Two General Characteristic Times of Transient Responses in Solid Oxide Cells. *Nat Commun* **2024**, *15* (1), 4587. https://doi.org/10.1038/s41467-024-48785-1.
(22) Ramadhani, F.; Hussain, M. A.; Mokhlis, H.; Hajimolana, S. Optimization Strategies for Solid Oxide Fuel Cell (SOFC) Application: A Literature Survey. *Renewable and Sustainable Energy Reviews* **2017**, *76*, 460–484. https://doi.org/10.1016/j.rser.2017.03.052.
(23) Feng, H.; Chen, L.; Xie, Z.; Sun, F. Constructal Optimization for a Single Tubular Solid Oxide Fuel Cell. *Journal of Power Sources* **2015**, *286*, 406–413. https://doi.org/10.1016/j.jpowsour.2015.03.162.

(24) Bhattacharyya, D.; Rengasamy, R.; Caine, F. Dynamic Simulation and Analysis of a Solid Oxide Fuel Cell (SOFC). *Computer Aided Chemical Engineering* **2007**. https://doi.org/10.1016/S1570-7946(07)80174-X.
(25) Cheddie, D. F. Thermo-Economic Optimization of an Indirectly Coupled Solid Oxide Fuel Cell/Gas Turbine Hybrid Power Plant. *International Journal of Hydrogen Energy* **2011**, *36* (2), 1702–1709. https://doi.org/10.1016/j.ijhydene.2010.10.089.
(26) Spivey, B. J.; Hedengren, J. D.; Edgar, T. F. Constrained Control and Optimization of Tubular Solid Oxide Fuel Cells for Extending Cell Lifetime. In *2012 American Control Conference (ACC)*; 2012; pp 1356–1361. https://doi.org/10.1109/ACC.2012.6315334.
(27) Gholaminezhad, I.; Jafarpur, K.; Paydar, M. H.; Karimi, G. Multi-Scale Multi-Objective Optimization and Uncertainty Analysis of Methane-Fed Solid Oxide Fuel Cells Using Monte Carlo Simulations. *Energy Conversion and Management* **2017**, *153*, 175–187. https://doi.org/10.1016/j.enconman.2017.10.011.
(28) de Avila Ferreira, T.; Wuillemin, Z.; Marchetti, A. G.; Salzmann, C.; Van Herle, J.; Bonvin, D. Real-Time Optimization of an Experimental Solid-Oxide Fuel-Cell System. *Journal of Power Sources* **2019**, *429*, 168–179. https://doi.org/10.1016/j.jpowsour.2019.03.025.
(29) Rauh, A. Kalman Filter-Based Real-Time Implementable Optimization of the Fuel Efficiency of Solid Oxide Fuel Cells. *Clean Technologies* **2021**, *3* (1), 206–226. https://doi.org/10.3390/cleantechnol3010012.
(30) Yin, R.; Sun, L.; Khosravi, A.; Malekan, M.; Shi, Y. Control-Oriented Dynamic Modeling and Thermodynamic Analysis of Solid Oxide Electrolysis System. *Energy Conversion and Management* **2022**, *271*, 116331. https://doi.org/10.1016/j.enconman.2022.116331.
(31) Cai, Q.; Adjiman, C. S.; Brandon, N. P. Optimal Control Strategies for Hydrogen Production When Coupling Solid Oxide Electrolysers with Intermittent Renewable Energies. *Journal of Power Sources* **2014**, *268*, 212–224. https://doi.org/10.1016/j.jpowsour.2014.06.028.
(32) Giridhar, N. V.; Allan, D. A.; Li, M.; Zitney, S. E.; Biegler, L. T.; Bhattacharyya, D. Optimal Operation of Solid-Oxide Electrolysis Cells Considering Long-Term Chemical Degradation. *Energy Conversion and Management* **2024**, *319*, 118950. https://doi.org/10.1016/j.enconman.2024.118950.
(33) Parhizkar, T.; Roshandel, R. Long Term Performance Degradation Analysis and Optimization of Anode Supported Solid Oxide Fuel Cell Stacks. *Energy Conversion and Management* **2017**, *133*, 20–30. https://doi.org/10.1016/j.enconman.2016.11.045.
(34) Giridhar, N. V.; Bhattacharyya, D.; Allan, D. A.; Zitney, S. E.; Li, M.; Biegler, L. T. Optimization of Solid Oxide Electrolysis Cell Systems Accounting for Long-Term Performance and Health Degradation. *Systems and Control Transactions* **2024**, 177040.
(35) Wang, Y.; Jiang, W.; Luo, Y.; Song, M.; Tu, S.-T. High Temperature Creep Strength Design and Optimization of Solid Oxide Fuel Cell. *International Journal of Hydrogen Energy* **2022**, *47* (50), 21450–21461. https://doi.org/10.1016/j.ijhydene.2022.04.261.
(36) Cheng, H.; Jing, S.; Xu, Y.; Deng, Z.; Li, J.; Li, X. Control-Oriented Modeling Analysis and Optimization of Planar Solid Oxide Fuel Cell System. *International Journal of Hydrogen Energy* **2016**, *41* (47), 22285–22304. https://doi.org/10.1016/j.ijhydene.2016.08.213.
(37) Li, M.; Allan, D. A.; Dinh, S.; Bhattacharyya, D.; Dabadghao, V.; Giridhar, N.; Zitney, S. E.; Biegler, L. T. Nonlinear Model Predictive Control for Mode-switching Operation of Reversible Solid Oxide Cell Systems. **2024**. https://doi.org/10.1002/aic.18550.
(38) Gao, Y.; Shi, T.; Yuan, Q.; Shi, X.; Sun, K. Particle Gradation Effects on Creep Characteristics and the Underlying Mechanism in Calcareous Sand. *Construction and Building Materials* **2024**, *424*, 135952. https://doi.org/10.1016/j.conbuildmat.2024.135952.
(39) Bahari, A.; Sadeghi-Nik, A.; Roodbari, M.; Sadeghi-Nik, A.; Mirshafiei, E. Experimental and Theoretical Studies of Ordinary Portland Cement Composites Contains Nano LSCO Perovskite with Fokker-Planck and Chemical Reaction Equations. *Construction and Building Materials* **2018**, *163*, 247–255. https://doi.org/10.1016/j.conbuildmat.2017.12.073.

(40) Soleimani Moghaddam, M.; Bahari, A.; Houshani, M.; Jafari, A.; Motallebi Tala Tapeh, S. A Review on Progress in the Field of Conditioning of Polymer Fuel Cell Stacks. *Journal of Power Sources* **2024**, *621*, 235300. https://doi.org/10.1016/j.jpowsour.2024.235300.
(41) Lee, A.; Ghouse, J. H.; Eslick, J. C.; Laird, C. D.; Siirola, J. D.; Zamarripa, M. A.; Gunter, D.; Shinn, J. H.; Dowling, A. W.; Bhattacharyya, D.; Biegler, L. T.; Burgard, A. P.; Miller, D. C. The IDAES Process Modeling Framework and Model Library—Flexibility for Process Simulation and Optimization. *Journal of Advanced Manufacturing and Processing* **2021**, *3* (3), e10095. https://doi.org/10.1002/amp2.10095.
(42) Laurencin, J.; Delette, G.; Lefebvre-Joud, F.; Dupeux, M. A Numerical Tool to Estimate SOFC Mechanical Degradation: Case of the Planar Cell Configuration. *Journal of the European Ceramic Society* **2008**. https://doi.org/10.1016/j.jeurceramsoc.2007.12.025.
(43) Hetnarski, R. B.; Eslami, M. R. *Thermal Stresses—Advanced Theory and Applications*; Solid Mechanics and Its Applications; Springer International Publishing: Cham, 2019; Vol. 158. https://doi.org/10.1007/978-3-030-10436-8.
(44) Kong, W.; Zhang, W.; Zhang, S.; Zhang, Q.; Su, S. Residual Stress Analysis of a Micro-Tubular Solid Oxide Fuel Cell. *International Journal of Hydrogen Energy* **2016**, *41* (36), 16173–16180. https://doi.org/10.1016/j.ijhydene.2016.05.256.
(45) Basu, B.; Tiwari, D.; Kundu, D.; Prasad, R. Is Weibull Distribution the Most Appropriate Statistical Strength Distribution for Brittle Materials? *Ceramics International* **2009**, *35* (1), 237–246. https://doi.org/10.1016/j.ceramint.2007.10.003.
(46) Clague, R.; Marquis, A. J.; Brandon, N. P. Time Independent and Time Dependent Probability of Failure of Solid Oxide Fuel Cells by Stress Analysis and the Weibull Method. *Journal of Power Sources* **2013**, *221*, 290–299. https://doi.org/10.1016/j.jpowsour.2012.07.116.
(47) Abhyankar, S.; Brown, J.; Constantinescu, E. M.; Ghosh, D.; Smith, B. F.; Zhang, H. PETSc/TS: A Modern Scalable ODE/DAE Solver Library. arXiv June 4, 2018. https://doi.org/10.48550/arXiv.1806.01437.
(48) Wächter, A.; Biegler, L. T. On the Implementation of an Interior-Point Filter Line-Search Algorithm for Large-Scale Nonlinear Programming. *Math. Program.* **2006**, *106* (1), 25–57. https://doi.org/10.1007/s10107-004-0559-y.
(49) Li, M.; Allan, D. A.; Dinh, S.; Bhattacharyya, D.; Dabadghao, V.; Giridhar, N.; Zitney, S. E.; Biegler, L. T. NMPC for Mode-Switching Operation of Reversible Solid Oxide Cell Systems. *AIChe Jounal* **2024**. https://doi.org/DOI: 10.1002/aic.18550.